In-flight Ice formation simulation on finite wings and air intakes

S. Özgen
sozgen@ae.metu.edu.tr
Middle East Technical University
Dept. Aerospace Engineering
Ankara, Turkey

M. Canıbek
mcanibek@tai.com.tr
Turkish Aerospace Industries
Flight Sciences Department
Ankara, Turkey

ABSTRACT

In the present article, in-flight ice formation on finite wings and air intakes of low-speed aircraft are numerically studied. The approach to the problem involves calculation of the velocity field using a three-dimensional panel method. Using the calculated velocity field, the droplet trajectories and droplet impact locations are computed yielding the droplet collection efficiency distribution. In the next step, convective heat transfer coefficient distributions around the geometries are calculated using a two-dimensional Integral Boundary-Layer Method, which takes surface roughness due to ice accretion into account. A thermodynamic analysis employing the Extended Messinger Method yields the ice growth rates. Integration of these rates over time yields the ice shapes, hence the modified geometry. Predicted ice shapes are compared with experimental shapes reported in the literature and good agreement is observed. Ice shapes around vastly varying geometries including complex shapes are successfully computed. As such, the developed tool may be used for academical purposes or for airworthiness certification efforts.

Paper No. 3595. Manuscript received 6 July 2010, revised version received 4 March 2011,
2nd revised version received 28 June 2011, accepted 18 August 2011.

NOMENCLATURE

Alphanumerical symbols

a_∞	speed of sound (ms^{-1})
A_p	droplet cross-sectional area (m^2)
B	ice thickness (m)
C_D	droplet drag coefficient
C_f	skin friction coefficient
C_p	specific heat of air (1,006J/kg.K)
C_{pi}	specific heat of ice (2,050J/kg.K)
C_{pw}	specific heat of water (4,218J/kg.K)
d_p	droplet median volume diameter (m)
D	drag force acting on a droplet (N)
e_o	saturation vapor pressure constant 27·03
F	fraction of wing or duct surface wetted by impinging droplets
g	gravitational acceleration (9·81m/s^2)
h	water layer thickness (m)
h_c	convective heat transfer coefficient (W/m^{2}s)
k_s	roughness height (m)
k	thermal conductivity of air (0·024W/m.K)*
k_i	thermal conductivity of ice (2·18W/m.K)
k_w	thermal conductivity of water (0·571W/m.K)
L_e	Lewis number (1/Pr)
L_E	latent heat of evaporation ($2{\cdot}50 \times 10^6$J/kg)
L_F	latent heat of solidification ($3{\cdot}344 \times 10^5$J/kg)
L_S	latent heat of sublimation ($2{\cdot}8344 \times 10^6$J/kg)
m	droplet mass (kg)
m_{in}	runback water mass flow rate (kg/m^{2}s)
me,s	mass flow rate of evaporting or sublimating water (kg/m^{2}s)
M	Mach number
Pr	laminar Prandtl number of air 0·72
P_{r_t}	turbulent Prandtl number of air 0·9
Q_x	energy terms
r	recovery factor
R	gas constant (J/kg.K)
Re	Reynolds number based on droplet properties
Re_k	roughness Reynolds number
St	Stanton number
St_k	roughness Stanton number
T	temperature (in the ice layer) (K)
T_a	ambient temperature (K)
T_f	freezing temperature (K)
T_s	wing or duct surface temperature (K)
t_{exp}	total icing time (exposure) (s)
U_e	flow velocity outside the boundary-layer (ms^{-1})

https://doi.org/10.1017/S000192400000525X Published online by Cambridge University Press

U_k Local flow velocity at the roughness height (ms^{-1})
V_x, V_y, V_z Flow velocity components at the droplet location (ms^{-1})
V_∞ Freestream velocity (ms^{-1})
V_{rel} Relative velocity between the droplets and the local flow (ms^{-1})
$\dot{x}_p, \dot{y}_p, \dot{z}_p$ Droplet velocity components (ms^{-1})
$\ddot{x}_p, \ddot{y}_p, \ddot{z}_p$ Droplet acceleration components (m/s^2)

Greek symbols

α angle-of-attack (°)
β droplet collection efficiency
δ boundary-layer thickness (m)
ε radiative surface emissivity of ice (0·5–0·8)
γ ratio of specific heats
$\gamma_1, \gamma_2, \gamma_3$ Angles between the droplet and flow velocity componentsdegrees
μ kinematic viscosity of ambient air (Pa.s*)
μ_w viscosity of wate (Pa.s*)
ν dynamic viscosity of air (m^2/s*)
ρ ambient density (kg/m^3*)
ρ_a liquid water content (kg/m^3)
ρ_r density of rime ice ($880kg/m^3$)
ρ_g density of glaze ice ($917kg/m^3$)
ρ_w density of water ($999kg/m^3$)
σ_r Stefan-Boltzmann constant ($5{\cdot}6704 \times 10^{-8}$)
σ_w surface tension of water (0·072N/m*)
τ shear stress (Pa)
θ temperature in the water layer (K)
θ_l laminar momentum thickness (m)
θ_t turbulent momentum thickness (m)

Subscripts

g glaze ice
i ice
l laminar
r rime ice
t turbulent
w water

* Temperature dependence is accounted for.

1.0 INTRODUCTION

Ice formation on airframe components such as wings, tail surfaces, engine intakes and nacelles during flight is a very serious flight safety issue. Presence of ice on airframe components modifies the geometry in an adverse manner; lift force decreases and the drag force increases, degrading the aerodynamic performance of the aircraft. Presence of ice on stabilisers and control surfaces result in severe and often unpredictable degradations in stability and control characteristics of

https://doi.org/10.1017/S000192400000525X Published online by Cambridge University Press

aircraft. Accumulated ice may block pitot tubes or other sensors resulting in false readings of flight parameters to the human pilot and/or the flight computer. An iced air intake will result in reduced mass flow of air into the engine, further degrading aircraft performance. Ice increases the weight of the aircraft, which increases the required thrust. Icing certification is one of the important issues in the whole certification process which is handled according to Federal Aviation Regulations, Part 25, §25.1419 (FAR 25) for transport category aircraft. Certification processes for other aircraft types closely follow the guidelines of FAR 25. Certification process involves flight and laboratory tests supplemented by numerical simulations.

An extensive overview of the literature related two-dimensional ice accretion simulation is given by Özgen and Canıbek[1]. Therefore, available literature only pertaining to three-dimensional simulations is presented here.

Myers[2] presents a one-dimensional mathematical model describing ice growth, which is an extension of the original Messinger model. It is shown that the model can also be extended to two and three-dimensions and it is the three-dimensional extension that is employed in the current study.

Potapczuk and Bidwell[3] report an effort to develop a three-dimensional ice accretion modelling. Three-dimensional flow field methods and droplet trajectories are combined with two-dimensional ice accretion calculations.

Mingione, Brandi and Saporiti[4] discuss a three-dimensional ice accretion code. Ice accretion on the NASA MS-317 30° swept wing and on the Agusta A109 air intake protection grid are evaluated.

Effect of ice formation on aircraft performance is studied by Cebeci and Besnard[5]. For specified flow conditions, the ice shapes on the leading edge of the lifting surfaces are computed by the LEWICE code developed by NASA.

In the experimental study of Papadakis *et al*[6], extensive small and large droplet impingement tests were conducted at the NASA Glenn Icing Research Tunnel (IRT). Impingement data were obtained for four aerofoil sections and two simulated ice shapes.

The present study is an effort to extend the previous work on two-dimensional analysis to three dimensions and to predict ice shapes on components of low-speed aircraft that are prone to in-flight icing. Therefore, the approach and the outline of the current study are very much similar to those of the two-dimensional approach reported by Özgen and Canıbek[1]. The major improvements realised when extending the two-dimensional numerical simulation to three dimensions can be summarised as follows:

- A three-dimensional panel method is used instead of a two-dimensional one for the flowfield solution. The components of the velocity vector at any point can be obtained with this approach, which are then used for determining the droplet trajectories.
- Droplet trajectories are computed by solving the dynamic equations for the droplets in three-dimensional form. In the two-dimensional simulation droplet impact on a surface is detected simply by detecting the intersection of a panel and a trajectory. However, in the three-dimensional simulation this method is not adequate and a impact detection method based on the area of a panel and a pyramid formed by the droplet and the panel is utilised as explained below.
- There is no difference between the two-dimensional and three-dimensional simulations in terms of the computation of the convective heat transfer coefficients. Both simulations use the two-dimensional Integral Boundary Layer equation. In the three-dimensional simulation it is implicitly assumed that at the leading edge of the wing where icing is most

https://doi.org/10.1017/S000192400000525X Published online by Cambridge University Press

likely to occur, the local boundary layer is still fairly two dimensional and there is no serious loss of accuracy due to this assumption.

- There is also no significant difference between the two-dimensional and three-dimensional simulations in terms of the implementation of the Extended Messinger Method. In the three-dimensional approach it is assumed that all runback water passes to the next downstream panel in the chordwise direction and there is no runback water effect in the spanwise direction. This assumption should not introduce significant inaccuracies for moderate and high aspect ratio wings with low and moderate sweep.

Using well-proven methods for velocity field, droplet trajectory, collection efficiency and ice accretion calculations, ice formation on five aerofoil/wing geometries and three air intake geometries are studied. To this end, a computer code is developed in FORTRAN programming language. Inputs to the problem are the ambient temperature T_a, freestream velocity V_∞, Liquid Water Content (LWC) of air ρ_a, droplet median volume diameter (MVD) d_p, total icing time t_{exp}, angle of attack α and the wing or intake geometry.

The analysis begins with the computation of the velocity field around the given geometry using a three-dimensional panel method. Using this information, local flow and droplet velocities can be calculated anywhere in the flow field, allowing calculations of the droplet trajectories. Each droplet trajectory starts at a plane sufficiently far upstream (typically ten chords upstream of the leading edge) and is computed by integrating three dimensional equations of motion in differential form. A particular trajectory computation ends either when the droplet impacts the geometry or passes beyond the trailing edge or rear end of the geometry without impacting it. The impact distribution yields the droplet collection efficiency distribution. For the thermodynamic analysis, heat transfer coefficients are calculated using the two-dimensional integral boundary-layer equation. Depending on ambient properties like temperature and liquid water content of air, rime ice, glaze ice or mixed ice forms on the surface. Rime ice typically occurs when the temperature and liquid water content of air is low, while glaze ice occurs when the conditions are milder and the liquid water content is relatively high. It has been shown that, glaze ice is always preceded by a thin layer of rime ice and the transition from rime to glaze ice is smooth. The extended Messinger Method employed in this study models this transition more faithfully compared to the original Messinger Method. Glaze ice is always accompanied by a thin layer of water over the ice layer, which under gravitational and/or aerodynamic forces, may flow downstream (called runback water) or be shed. It is also probable that some parts of the geometry are covered by rime ice and the remaining by glaze ice, resulting in mixed ice formation.

The developed computational tool allows simulations to be performed either in one-layer mode, where the ice shapes are predicted in one step for the entire exposure duration t_{exp}, or in multi-layer mode where t_{exp} is divided into segments (or layers). In the multi-layer mode, flowfield, droplet trajectory and icing calculations are repeated for each layer. This approach allows the effect of ice shapes on flowfield and droplet trajectories to be taken into account, thus reflecting the physics of the problem more realistically. Also cases involving varying ambient and icing conditions can be treated, like climbing or descending flights.

In the following, Section 2 describes the solution method, where flow field, droplet trajectory, droplet collection efficiency and convective heat transfer coefficient calculations, and the Extended Messinger Method are briefly introduced. Icing intensity definitions are also included this section. In Section 3, the results obtained for five aerofoil/wing and three intake geometries are presented, which also include a validation check. The results are also interpreted in terms of icing intensity definitions. Important inferences of the study, recommendations for future work and concluding remarks constitute Section 5.

https://doi.org/10.1017/S000192400000525X Published online by Cambridge University Press

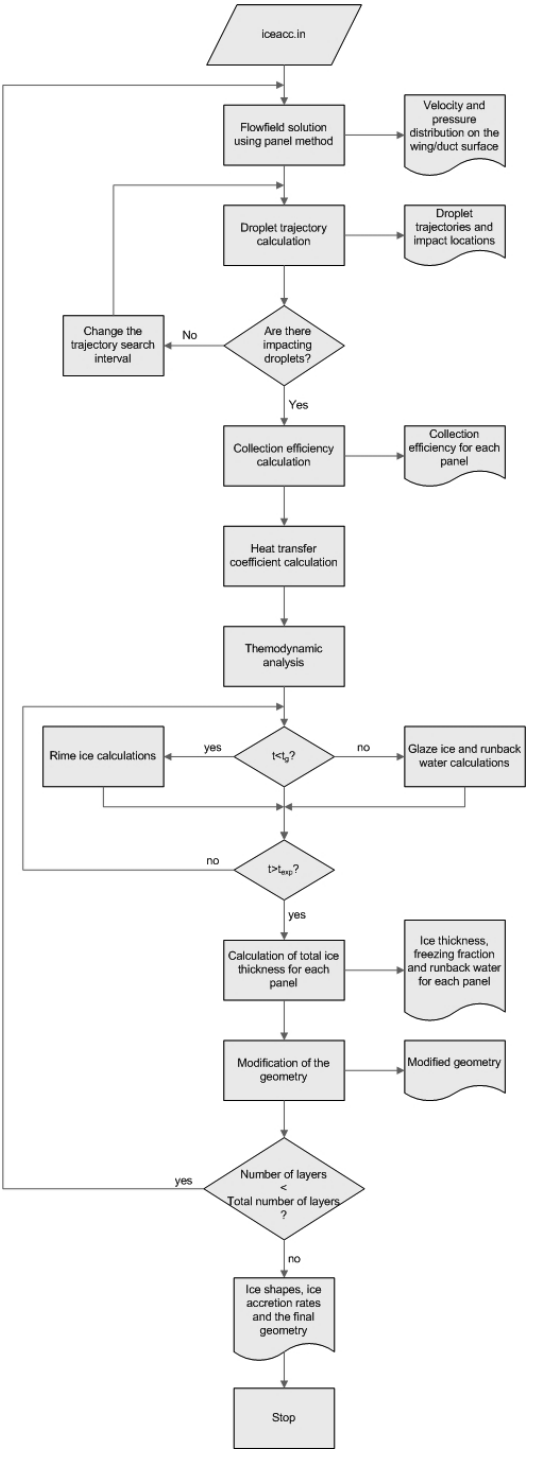

Figure 1. Flowchart of the present calculation procedure.

https://doi.org/10.1017/S000192400000525X Published online by Cambridge University Press

2.0 PROBLEM FORMULATION AND SOLUTION METHOD

In this Section, the method developed for ice accretion calculations applicable to three-dimensional geometries is summarised. A brief flowchart of the calculation procedure and the developed program is presented in Fig. 1, repeated from Özgen and Canıbek[1].

2.1 Flow field solution: Three-dimensional panel method

In order to compute the air flow velocity components so that the droplet trajectories can be calculated, a panel method is utilised[7]. In this method, the wing or intake geometry is divided into quadrilateral panels each associated with a singularity element. The strengths of the singularities are taken to be constants and are unknowns of the problem. The developed computer program uses N quadrilateral panels to solve for N singularity strengths using the flow tangency boundary condition at the collocation points of the panels. The collocation points are the centroids of each panel. Once the singularity strengths are calculated, one can construct a velocity potential and hence calculate the air flow velocity components at any location in the flow field. The velocity components at a given point are the x-, y- z-derivatives of the velocity potential constructed at that point. The results of the panel method also serve the boundary-layer calculations, for which the inviscid velocity distribution around the geometry is required. The boundary layer calculations are performed in order to calculate the convective heat transfer distribution around the geometry.

Although some authors have used higher-order flow solvers such as Navier-Stokes calculations in order to obtain the air flow velocity components, it is reported that no additional accuracy is obtained that would justify the vastly increased computational time[8,9].

2.2 Droplet trajectories and the collection efficiencies

For small droplets i.e. $d_p \leq 500\mu m$, the following assumptions are employed for droplet trajectory computations:

- Droplets are assumed to be spherical due to their small size,
- The presence of the droplets do not affect the flow field,
- Gravity and aerodynamic drag acting on the droplets are the only forces considered.

According to Jeck[10], droplet sizes larger than 25μm are rare (less than 4% in all icing encounters); therefore the above assumptions are valid for the purposes of this study.

The equations that define the motion of the droplets are:

$$m\ddot{x}_p = -(D\mathrm{Cos}\gamma_1) \quad \ldots (1)$$

$$m\ddot{y}_p = -(D\mathrm{Cos}\gamma_2) \quad \ldots (2)$$

$$m\ddot{z}_p = -(D\mathrm{Cos}\gamma_3 + mg) \quad \ldots (3)$$

with

$$\gamma_1 = \mathrm{Tan}^{-1}\frac{\dot{x}_p - V_x}{V_{rel}}, \quad \gamma_2 = \mathrm{Tan}^{-1}\frac{\dot{y}_p - V_y}{V_{rel}}, \quad \gamma_3 = \mathrm{Tan}^{-1}\frac{\dot{z}_p - V_z}{V_{rel}}, \quad \ldots (4)$$

https://doi.org/10.1017/S000192400000525X Published online by Cambridge University Press

$$D = \tfrac{1}{2}\rho V_{rel}^2 C_D A_p, \qquad \ldots (5)$$

$$V_{rel} = \sqrt{\left(\dot{x}_p - V_x\right)^2 + \left(\dot{y}_p - V_y\right)^2 + \left(\dot{z}_p - V_z\right)^2}. \qquad \ldots (6)$$

In the above equations, V_x, V_y and V_z are the components of the flow velocity at the droplet location, while $\dot{x}_p, \dot{y}_p, \dot{z}_p, \ddot{x}_p, \ddot{y}_p, \ddot{z}_p$ are the components of the droplet velocity and acceleration. The symbols ρ and A_p denote the atmospheric density and cross-sectional area of the droplet. C_D denotes the droplet drag coefficient. It is calculated using the drag law for spherical droplets given by Clift *et al*[11]:

$$\begin{aligned}
&\mathrm{Re} \le 0{\cdot}01, && C_D = \frac{9}{2} + \frac{24}{\mathrm{Re}} \\
&0{\cdot}01 \le \mathrm{Re} \le 20, && C_D = \frac{24}{\mathrm{Re}}\left[1 + 0{\cdot}1315\,\mathrm{Re}^{(0{\cdot}82 - 0{\cdot}05w)}\right] \\
&20 \le \mathrm{Re} \le 260, && C_D = \frac{24}{\mathrm{Re}}\left[1 + 0{\cdot}1935\,\mathrm{Re}^{0{\cdot}6305}\right] \\
&260 \le \mathrm{Re} \le 1{,}500, && \log_{10} C_D = 1{\cdot}6435 - 1{\cdot}1242w + 0{\cdot}1558w^2 \\
&1{,}500 \le \mathrm{Re} \le 12{,}000 && \log_{10} C_D = -2{\cdot}4571 + 2{\cdot}5558w - 0{\cdot}9295w^2 + 0{\cdot}10 \\
&12{,}000 \le \mathrm{Re} \le 44{,}000 && \log_{10} C_D = -1{\cdot}9181 + 0{\cdot}637w - 0{\cdot}0636w^2 \\
&44{,}000 \le \mathrm{Re} \le 338{,}000 && \log_{10} C_D = -4{\cdot}339 + 1{\cdot}5809w - 0{\cdot}1546w^2 \\
&33{,}8000 \le \mathrm{Re} \le 400{,}000 && C_D = 29{\cdot}78 - 5{\cdot}3w \\
&400{,}000 \le \mathrm{Re} \le 10^6 && C_D = 0{\cdot}1w - 0{\cdot}49 \\
&\mathrm{Re} > 10^6 && C_D = 0{\cdot}19 - \frac{80{,}000}{\mathrm{Re}}
\end{aligned} \qquad \ldots (7)$$

In the above formulation, $\mathrm{Re} = \rho V_{rel} d_p / \mu$ is the Reynolds number based on droplet diameter d_p and relative velocity V_{rel}, while μ is the atmospheric viscosity. The viscosity is calculated using Sutherland's law as a function of temperature, given by Schlichting[12]. An example to the results of the trajectory calculations are shown in Fig. 2 for a wing geometry.

The droplet impact on the surface is detected as follows. A pyramid is constructed such that the panel on the wing surface is the base of the pyramid as shown in Fig. 3. As a droplet approaches a panel, the sum of the areas of the four sides (A_s) of the pyramid approaches to that of its base (A_b). The criterion for impact is as follows:

$$\frac{\left|A_s - A_b\right|}{A_b} \le 10^{-3}. \qquad \ldots (8)$$

The droplet impact distribution on the geometry determines the amount of water that impacts the surface and the probability of ice growth. The local collection efficiency is defined as the ratio of the area of impingement to the area through which droplets pass at some distance upstream of the geometry. The local collection efficiency can be expressed as:

$$\beta = \frac{A_o}{A}, \qquad \ldots (9)$$

https://doi.org/10.1017/S000192400000525X Published online by Cambridge University Press

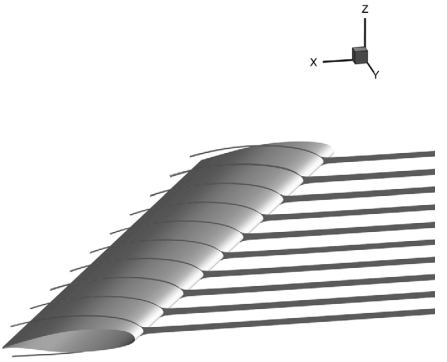

Figure 2. Droplet trajectories for the NASA MS-317 30º swept wing, V_∞= 74ms^2, α = 4º, T_a = –18·1ºC.

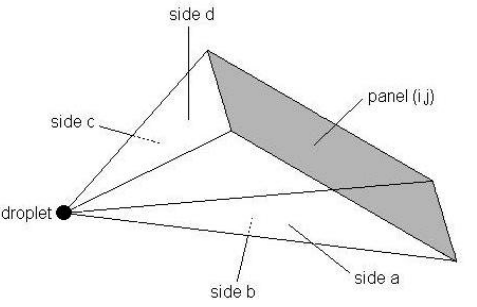

Figure 3. Determination of droplet impact.

where A_o is the area constituted by four droplets in the release plane, while A is the area on the geometry constituted by the same four droplets after impact. In the developed computer program, the collection efficiencies are calculated for nodes where the ice growth rates are to be calculated, which happen to be the vertices of the panels. Figure 4 illustrates how the collection efficiencies are calculated and Fig. 5 shows a typical distribution. As can be seen, the droplet collection efficiency attains its maximum value around the stagnation line and decreases in the streamwise direction on both the upper and lower surfaces. The dependence of the droplet collection efficiency to geometry size, droplet size, velocity and angle of attack are discussed by Özgen and Canıbek[1].

In the developed computer program, droplet trajectory calculations consume more than 99% of all CPU time. In a multi-layer calculation, as the droplet calculations are repeated for each layer, total CPU time is roughly equal to the number of layers multiplied by the CPU time for a single layer calculation. Developing a parallel-computing technique in order to calculate the droplet trajectories would significantly reduce the CPU time.

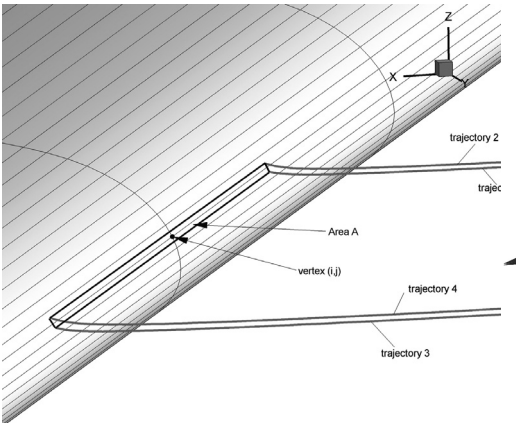

Figure 4. Calculation of droplet collection efficiencies.

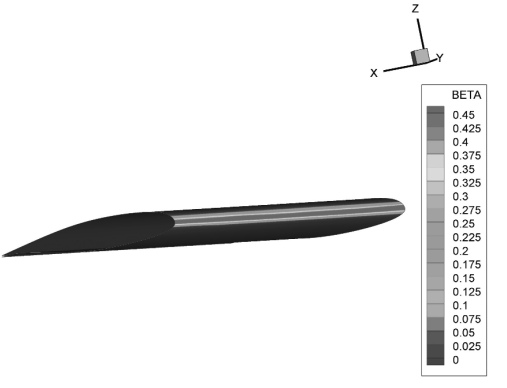

Figure 5. Droplet collection efficiency distribution on the NASA MS-317 30º swept wing, V_∞= 74ms^2, α = 4º, T_a = –18·1ºC.

https://doi.org/10.1017/S000192400000525X Published online by Cambridge University Press

2.3 Calculation of convective heat transfer coefficients

When the collection efficiency distribution around the geometry is determined, the convective heat transfer coefficients need to be determined for the thermodynamical analysis. The geometry is divided into strips and boundary-layer calculations are performed for each of these strips by solving the two-dimensional Integral Boundary Layer equation. The boundary-layer calculations start at the stagnation point at the leading edge and proceed downstream using the marching technique for the upper and lower surfaces of the wing or duct. This method enables calculation of the details of the laminar and turbulent boundary layers fairly accurately. Since a two-dimensional approach is used, the same method used by Özgen and Canıbek[1] can be adopted for this problem. The following discussion is repeated from the aforementioned study.

Transition prediction is based on the roughness Reynolds number, $\mathrm{Re}_k = \rho U_k k_s/\mu$, where k_s is the roughness height in mm and U_k is the local flow velocity at the roughness height. Transition from laminar to turbulent flow occurs at the streamwise location where $\mathrm{Re}_k = 600$, according to Von Doenhoff criterion. The flow velocity at the roughness height is calculated from Paraschiviou and Saeed[8]:

$$\frac{U_k}{U_e} = 2\frac{k_s}{\delta} - 2\left(\frac{k_s}{\delta}\right)^3 + \left(\frac{k_s}{\delta}\right)^4 + \frac{1}{6}\frac{\delta^2}{\nu}\frac{\mathrm{d}U_e}{\mathrm{d}s}\frac{k_s}{\delta}\left(1-\frac{k_s}{\delta}\right)^3. \quad \ldots (10)$$

In the above expression, U_e is the flow velocity outside the boundary-layer at the roughness location. Roughness height is calculated from[13]:

$$k_s = (4\sigma_w \mu_w / \rho_w F\tau)^{1/3} \quad \ldots (11)$$

where σ_w, ρ_w and μ_w denote the surface tension, density and viscosity of water, respectively. Fraction of the wing or duct surface that is wetted by water droplets is expressed by F, while τ denotes local surface shear stress. The laminar boundary layer thickness is given by[12]:

$$\delta = \frac{315}{37}\theta_l. \quad \ldots (12)$$

Laminar momentum thickness is computed using Thwaites' formula[12]:

$$\frac{\theta_l^2}{\nu} = \frac{0\cdot 45}{U_e^6}\int_0^s U_e^5 \mathrm{d}s. \quad \ldots (13)$$

In the above expression and s is the streamwise distance along the wing or duct surface measured with respect to the stagnation point. For laminar flow $\mathrm{Re}_k \le 600$, the equation of Smith and Spalding is employed to calculate the convective heat transfer coefficient[14]:

$$h_c = \frac{0\cdot 296 k U_e^{1.435}}{\sqrt{\nu\int_0^s U_e^{1.87}\mathrm{d}s}}, \quad \ldots (14)$$

where k is the conductivity of air. The conductivity of air is temperature-dependent and is calculated by using viscosity computed from Sutherland's viscosity law with Prandtl number and specific heat assumed constant. Notice that expression (14) is independent of the roughness height.

https://doi.org/10.1017/S000192400000525X Published online by Cambridge University Press

For turbulent flow $Re_k > 600$, the method of Kays and Crawford is employed[14]. The turbulent convective heat transfer coefficient is evaluated by using:

$$h_c = St\rho U_e C_p \quad \ldots (15)$$

where C_p is the specific heat of air.
The Stanton number can be calculated from:

$$\mathrm{St} = \frac{C_f/2}{\mathrm{Pr_t} + \sqrt{(C_f/2)/\mathrm{St_k}}}, \quad \ldots (16)$$

where $\mathrm{Pr}_t = 0{\cdot}9$ is the turbulent Prandtl number. The roughness Stanton number is given as:

$$\mathrm{St_k} = 1{\cdot}92\,\mathrm{Re_k^{-0{\cdot}45}}\,\mathrm{Pr^{-0{\cdot}8}}, \quad \ldots (17)$$

where $\mathrm{Pr} = \mu C_p/k = 0{\cdot}72$ is the laminar Prandtl number. The skin friction is calculated by using the Makkonen relation:

$$\frac{C_f}{2} = \frac{0{\cdot}1681}{\left[\ln(864\theta_t/k_s + 2{\cdot}568)\right]^2}. \quad \ldots (18)$$

The turbulent momentum thickness is computed from:

$$\theta_t = \frac{0{\cdot}036\nu^{0{\cdot}2}}{U_e^{3{\cdot}29}}\left(\int_{s_{tr}}^{s} U_e^{3{\cdot}86}\,ds\right)^{0{\cdot}8} + \theta_{tr}, \quad \ldots (19)$$

where θ_{tr} is the laminar momentum thickness at the transition location.

2.4 Extended Messinger model

The ice prediction approach employed in this study is essentially the same as the one used by Özgen and Canıbek[1], extended to handle ice formation on three-dimensional geometries. Therefore; the definitions below are mostly repeated from that study. The ice shape prediction is based on the standard method of phase change or the Stefan problem. The phase change problem is governed by four equations: energy equations in the ice and water layers, mass conservation equation and a phase change condition at the ice/water interface[2]:

$$\frac{\partial T}{\partial t} = \frac{k_i}{\rho_i C_{pi}}\frac{\partial^2 T}{\partial y^2}, \quad \ldots (20)$$

$$\frac{\partial \theta}{\partial t} = \frac{k_w}{\rho_w C_{pw}}\frac{\partial^2 \theta}{\partial y^2}, \quad \ldots (21)$$

$$\rho_i \frac{\partial B}{\partial t} + \rho_w \frac{\partial h}{\partial t} = \rho_a \beta V_\infty + \dot{m}_{in} - \dot{m}_{e,s}, \quad \ldots (22)$$

$$\rho_i L_F \frac{\partial B}{\partial t} = k_i \frac{\partial T}{\partial y} - k_w \frac{\partial \theta}{\partial y}, \quad \ldots (23)$$

https://doi.org/10.1017/S000192400000525X Published online by Cambridge University Press

where θ and T are the temperatures, k_w and k_i are the thermal conductivities, C_{pw} and C_{pi} are the specific heats and h and B are the thicknesses of water and ice layers, respectively. In Equation (22), $\rho_a \beta V_\infty$, m_{in} and $\dot{m}_{e,s}$ are impinging, runback and evaporating (or sublimating) water mass flow rates for a control volume (panel), respectively. In Equation (23), ρ_i and L_F denote the density of ice and the latent heat of solidification of water, respectively. Ice density is assumed to have two different values for rime ice (ρ_r) and glaze ice (ρ_g). The co-ordinate y is normal to the surface. In order to determine the ice and water thicknesses together with the temperature distribution at each layer, boundary and initial conditions must be specified. These are based on the following assumptions[2]:

1. Ice is in perfect contact with the wing or duct surface:

$$T(0,t) = T_S \qquad \ldots (24)$$

The surface temperature is taken to be the recovery temperature[14]:

$$T_s = T_a + \frac{V_\infty^2 - U_e^2}{2C_p} \frac{1 + 0 \cdot 2rM^2}{1 + 0 \cdot 2M^2}. \qquad \ldots (25)$$

In the above expression, M is the flow Mach number given as $M = V_\infty / a_\infty$, while $a_\infty = \sqrt{\gamma R T_a}$ is the speed of sound. Additionally, r is the adiabatic recovery factor ($r = Pr^{1/2}$ for laminar flow, $r = Pr^{1/3}$ for turbulent flow).

2. The temperature is continuous at the ice/water boundary and is equal to the freezing temperature:

$$T(B, t) = \theta(B, t) = T_f \qquad \ldots (26)$$

3. At the air/water (glaze ice) or air/ice (rime ice) interface, heat flux is determined by convection (Q_c), radiation (Q_r), latent heat release (Q_l), cooling by incoming droplets (Q_d), heat brought in by runback water (Q_{in}), evaporation (Q_e) or sublimation (Q_s), aerodynamic heating (Q_a) and kinetic energy of incoming droplets (Q_k):

Glaze ice: $$-k_w \frac{\partial \theta}{\partial y} = \left(Q_c + Q_e + Q_d + Q_r\right) - \left(Q_a + Q_k + Q_{in}\right) \quad \text{at} \quad y = B + h. \qquad \ldots (27)$$

Rime ice: $$-k_i \frac{\partial T}{\partial y} = \left(Q_c + Q_s + Q_d + Q_r\right) - \left(Q_a + Q_k + Q_{in} + Q_l\right) \quad \text{at} \quad y = B. \qquad \ldots (28)$$

4. Wing or duct surface is initially clean:

$$B = h = 0, \quad t = 0 \qquad \ldots (29)$$

In the current approach, each panel constituting the geometry is also a control volume. The above equations are written for each panel and ice is assumed to accumulate perpendicularly to a panel. This is an extension of the one-dimensional model described by Myers[2] to three-dimensional, which is done by taking mass and energy terms due to runback water flow in the conservation equations into account, see Equation (22).

2.4.1 Rime ice growth and temperature profile

Rime ice thickness can be obtained directly from the mass conservation Equation (22) as water droplets freeze immediately on impact, i.e. $h = 0$[2]:

https://doi.org/10.1017/S000192400000525X Published online by Cambridge University Press

$$B(t) = \frac{\rho_a \beta V_\infty + \dot{m}_{in} - \dot{m}_s}{\rho_r} t. \quad \ldots (30)$$

It has been shown that, for ice thicknesses less than 2·4cm (which the case for most applications), the temperature distribution is governed by[2]:

$$\frac{\partial^2 T}{\partial y^2} = 0. \quad \ldots (31)$$

Integrating the above equation twice and applying the boundary and interface conditions given in Equations (24) and (26) results in the temperature distribution in the rime ice layer:

$$T(y) = T_s + \frac{(Q_a + Q_k + Q_{in} + Q_l) - (Q_c + Q_d + Q_s + Q_r)}{k_i} y. \quad \ldots (32)$$

2.4.2 Glaze ice growth

It has been shown that, if ice and water layer thicknesses are less than 2·4cm and 3mm (which is the case for most applications), respectively, the temperature distributions in the ice and water layers are governed by the following equations[2]:

$$\frac{\partial^2 T}{\partial y^2} = 0, \quad \frac{\partial^2 \theta}{\partial y^2} = 0. \quad \ldots (33)$$

After integrating above equation twice and employing the conditions (24) and (26), the temperature distribution in the ice layer becomes:

$$T(y) = \frac{T_f - T_s}{B} y + T_s. \quad \ldots (34)$$

The temperature distribution in the water layer is obtained by integrating equation (33) twice and employing the interface conditions (26) and (27):

$$\theta(y) = T_f + \frac{(Q_a + Q_k + Q_{in}) - (Q_c + Q_d + Q_e + Q_r)}{k_w} (y - B). \quad \ldots (35)$$

Integrating mass conservation Equation (22) yields the water height, h:

$$h = \frac{\rho_a \beta V_\infty + \dot{m}_{in} - \dot{m}_e}{\rho_w} (t - t_g) - \frac{\rho_g}{\rho_w} (B - B_g), \quad \ldots (36)$$

where B_g is the rime ice thickness at which glaze ice first appears and t_g is the time at which this happens. When Equation (36) is substituted into the phase change condition in Equation (23), a first order ordinary differential equation for the ice thickness is obtained:

$$h = \frac{\rho_a \beta V_\infty + \dot{m}_{in} - \dot{m}_e}{\rho_w} (t - t_g) - \frac{\rho_g}{\rho_w} (B - B_g), \quad \ldots (37)$$

In order to calculate the glaze ice thickness as a function of time, Equation (37) is integrated numerically, using a Runge-Kutta-Fehlberg method.

https://doi.org/10.1017/S000192400000525X Published online by Cambridge University Press

During transition from rime ice to glaze ice, ice growth rate must be continuous:

$$\left.\frac{\partial B}{\partial t}\right)_{rime} = \left.\frac{\partial B}{\partial t}\right)_{glaze} \text{ at } B = B_g \text{ or } t = t_g. \quad \ldots (38)$$

Using Equations (30) and (37) yields:

$$B_g = \frac{k_i\left(T_f - T_s\right)}{\left(\rho_a \beta V_\infty + \dot{m}_{in} - \dot{m}_{sub}\right)L_F + \left(Q_a + Q_k + Q_{in}\right) - \left(Q_c + Q_d + Q_e + Q_r\right)}, \quad \ldots (39)$$

$$t_g = \frac{\rho_r}{\rho_a \beta V_\infty + \dot{m}_{in} - \dot{m}_{sub}} B_g. \quad \ldots (40)$$

Notice that Equation (39) may yield negative or positive values of B_g, such as:

- $B_g \geq 0$ Equation (39) yields the ice thickness when glaze ice first appears. Consequently, Equation (40) yields the time at which this happens.
- $B_g < 0$ indicates that glaze ice will not appear. This may be due to two reasons:
  - o $T_f - T_s < 0$ indicating that the substrate is too warm for ice to grow.
  - o The denominator of Equation (39) is less than zero meaning that there is insufficient energy to produce liquid water and pure rime ice is produced.

2.4.3 Energy terms

The energy terms appearing in the above equations need to be expressed in terms of the field variables. Although convective heat transfer (Q_c) and latent heat (Q_l) are the most prominent terms, all relevant energy terms are considered and used in the developed computer program. In the following, Tsur is the temperature at the ice (rime ice) or water surface (glaze ice).

- Convective heat transfer at the water surface (Q_c):

$$Q_c = h_c(T_{sur} - T_a) \quad \ldots (41)$$

- Cooling by incoming droplets (Q_d):

$$Q_d = \rho_a \beta V_\infty C_{pw}(T_{sur} - T_a) \quad \ldots (42)$$

- Evaporative heat loss (Q_e):

$$Q_e = \chi_e e_o\,(T_{sur} - T_a) \quad \ldots (43)$$

where χ_e is the evaporation coefficient and $e_o = 27{\cdot}03$.

Evaporation coefficient is expressed as[2]:

$$\chi_e = \frac{0{\cdot}622 h_c L_E}{C_p P_t L e^{2/3}}, \quad \ldots (44)$$

where P_t is the total pressure of the airflow.

https://doi.org/10.1017/S000192400000525X Published online by Cambridge University Press

- Sublimation heat loss (Q_s):

$$Q_s = \chi_s e_o (T_{sur} - T_a), \quad \ldots (45)$$

Sublimation coefficient χ_s is expressed as[2]:

$$\chi_s = \frac{0 \cdot 622 h_c L_S}{C_p P_l Le^{2/3}} \cdot \quad \ldots (46)$$

- Heat loss due to radiation (Q_r)[15]:

$$Q_r = 4\varepsilon\sigma_r T_a^3 (T_{sur} - T_a), \quad \ldots (47)$$

where ε is the surface emissivity and σr is the Stefan-Boltzmann constant.

- Aerodynamic heating term (Q_a):

$$Q_a = \frac{r h_c V_\infty^2}{2C_p}, \quad \ldots (48)$$

- Kinetic energy of incoming droplets (Q_k):

$$Q_k = \rho_a \beta V_\infty \frac{V_\infty^2}{2}, \quad \ldots (49)$$

- Energy brought in by runback water (Q_{in}):

$$Q_{in} = \dot{m}_{in} C_{pw} (T_f - T_{sur}), \quad \ldots (50)$$

where $\dot{m}_{in}$ is the mass flow rate of the incoming runback water.

- Latent heat of solidification (Q_l):

$$Q_l = \rho_r L_F \frac{\partial B}{\partial t}. \quad \ldots (51)$$

With these definitions, it is possible to express Equations (32), (35), (37) and (39) in terms of the surface temperature of the geometry (T_s) and ambient temperature (T_a) only.

2.4.4 Rime ice temperature distribution

Equation (32) can be written as:

$$T(y) = \frac{Q_{0r} - Q_{1r} T_s}{k_i + Q_{1r} B} y + T_s, \quad \ldots (52)$$

where

$$Q_{0r} = \rho_r L_F \frac{\partial B}{\partial t} + \rho_a \beta V_\infty \frac{V_\infty^2}{2} + r h_c \frac{V_\infty^2}{2C_{pa}} + \rho_a \beta V_\infty C_{pw} T_a + h_c T_a \quad \ldots (53)$$

https://doi.org/10.1017/S000192400000525X Published online by Cambridge University Press

$$Q_{1r} = \rho_a \beta V_\infty C_{pw} + h_c + 4\varepsilon\sigma_r T_\infty^3 + \chi_s e_0 + \dot{m}_{in} C_{pw.} \quad \ldots (54)$$

2.4.5 Glaze ice temperature distribution and ice growth rate

Equation (35) can be written as:

$$\theta(y) = \frac{Q_0 - Q_1 T_f}{k_w + Q_1 h} h + T_f, \quad \ldots (55)$$

where

$$Q_0 = \rho_a \beta V_\infty \frac{V_\infty^2}{2} + r h_c \frac{V_\infty^2}{2C_{pa}} + \rho_a \beta V_\infty C_{pw} T_a + h_c T_a + 4\varepsilon\sigma_r T_a^4 + \chi_e e_0 T_a + \dot{m}_{in} C_{pw} T_f, \quad \ldots (56)$$

$$Q_1 = \rho_a \beta V_\infty C_{pw} + h_c + 4\varepsilon\sigma_r T_\infty^3 + \chi_e e_0 + \dot{m}_{in} C_{pw.} \quad \ldots (57)$$

Equation (37) can be written as:

$$\rho_g L_F \frac{\partial B}{\partial t} = k_i \frac{T_f - T_s}{B} - k_w \frac{Q_0 - Q_1 T_f}{k_w + Q_1 h}. \quad \ldots (58)$$

Equation (39) can be written as:

$$B_g = \frac{k_i \left(T_f - T_s\right)}{\rho_g L_F \left(\frac{\rho_a \beta V_\infty + \dot{m}_{in} - \dot{m}_{sub}}{\rho_r}\right) + \left(Q_0 - Q_1 T_f\right)}. \quad \ldots (59)$$

2.4.6 Freezing fractions and runback water

Freezing fraction for a given control volume (or a panel in this case) is the ratio of the amount of water that solidifies to the amount of water that impinges on the control volume plus the water that enters the panel as runback water.

Rime ice: $$FF = \frac{\rho_r B}{\left(\rho_a \beta V_\infty + \dot{m}_{in}\right) t}. \quad \ldots (60)$$

Glaze ice: $$FF = \frac{\rho_r B_g + \rho_g \left(B - B_g\right)}{\left(\rho_a \beta V_\infty + \dot{m}_{in}\right) t}. \quad \ldots (61)$$

Runback water mass flow rate:

$$\dot{m}_{out} = \left(1 - FF\right)\left(\rho_a \beta V_\infty + \dot{m}_{in}\right) - \dot{m}_e. \quad \ldots (62)$$

This becomes $\dot{m}_{in}$ for the neighboring downstream panel. It is assumed that, all unfrozen water passes to the next downstream panel for the upper surface of the geometry. For the lower surface, it is assumed that all the unfrozen water is shed[16].

https://doi.org/10.1017/S000192400000525X Published online by Cambridge University Press

2.4.7 Evaporating or sublimating mass

Evaporating mass is given as:

$$\dot{m}_e = \frac{Q_E}{L_E}. \quad \ldots (63)$$

Likewise, sublimating mass is expressed as:

$$\dot{m}_s = \frac{Q_S}{L_S}. \quad \ldots (64)$$

2.5 Icing intensity definitions

The definitions for icing intensity as proposed by Jeck[10] are employed in order to add another dimension to the interpretation of the results and to provide further insight. According to the definition, the accumulation time of a quarter inch of ice (roughly 6mm) on the geometry determines the icing intensity. These definitions are summarised in Table 1.

Table 1
Icing intensity definitions as proposed by Jeck[10]

Icing intensity	Time to accumulate 0·25″ of ice
Trace	> 1 hour
Light	15 to 60 minutes
Moderate	5 to 15 minutes
Intense	< 5 minutes

3.0 RESULTS FOR AEROFOIL AND WING GEOMETRIES, CODE VALIDATION

The developed tool is validated with ice shapes obtained from experimental and numerical studies available in the literature. Eight test cases are selected such that the effects of geometry, ambient and icing conditions on ice formation and the degree at which the code is able to predict these are assessed. Geometric and ambient conditions, as well as icing data for these cases are presented for two-dimensional and three-dimensional geometries in Tables 2 and 3, respectively. Since experimental and numerical ice data for three-dimensional geometries are extremely scarce in the literature, aerofoil data is used in Figs 6, 7, 8 and 9. Two-dimensional test cases are selected from the literature such that the resulting ice shapes are complex, i.e. displaying single or double horns and the effects of compressibility are prominent[13]. In the computations, the span of the wing is chosen to be ten times its chord in order to simulate the flow over an aerofoil, and the ice data is taken from a spanwise section close to the symmetry plane of the wing in order to approach the aerofoil flow conditions further. In each calculation, 149 chordwise and 8 spanwise panels are used. Different panel numbers are also tested but the chosen combination seems to be a good compromise between accuracy and computational time as no significant accuracy is gained by using 199 chordwise and 16 spanwise panels, for example. Also, the multi-layer approach is used, where the total exposure time is divided into four layers in all subsequent computations.

https://doi.org/10.1017/S000192400000525X Published online by Cambridge University Press

Table 2
Geometric characteristics and flow conditions for code validation (2D)

Variable	Value			
	Case 31[13]	Case 34[13]	Case 35[13]	Case 39[13]
α, angle-of-attack (°)	4	4	4	0
c, wing chord or duct length (m)	0·53	0·53	0·53	0·465
V_∞, freestream velocity (ms^{-1})	58·1	93·9	93·9	131·5
ρ_∞, ambient pressure (Pa)	95,610·	92,060·	92,060·	85,000·
T_a, ambient temperature (°C)	–3·9	–16·6	–12·2	–3·9
ρ_a, liquid water content (g/m^3)	1·3	1·05	1·05	0·6
t_{exp}, exposure time (s)	480	372	372	180
d_p, droplet diameter (μm)	20	20	20	20

Figure 6 illustrates the results of the analysis for a high temperature case, where the ice formation is mostly glaze with runback water effects. As can be seen, the extent of the ice both on the upper and lower surface is well predicted in the current study compared with the experimental ice shape. Also the prominent bump and its position on the upper surface are reproduced by the computations, although underestimated in size. Moreover, the second bump just downstream of the prominent bump has also been well captured. The size and distribution of the ice formation on the lower surface is reproduced with accuracy in the current study. The maximum ice thickness is 1·1cm suggesting that the icing conditions are moderate in terms of icing intensity when the exposure time is considered. Meanwhile, the overall ice volume is slightly underestimated by the current computations. On the other hand, the numerical results obtained from fully two-dimensional computations by other investigators overpredict the extent of the iced region on the upper surface and the bumps on the upper surface are not fully reproduced. This suggests that runback water is overpredicted by other studies and the current study is slightly superior in that respect. However, it has to be kept in mind that all the numerical results that are used here for comparison date back to 1997 and the computational tools that are used for obtaining them almost certainly must have evolved over time and the current results would probably be in much better agreement with the experimental results now.

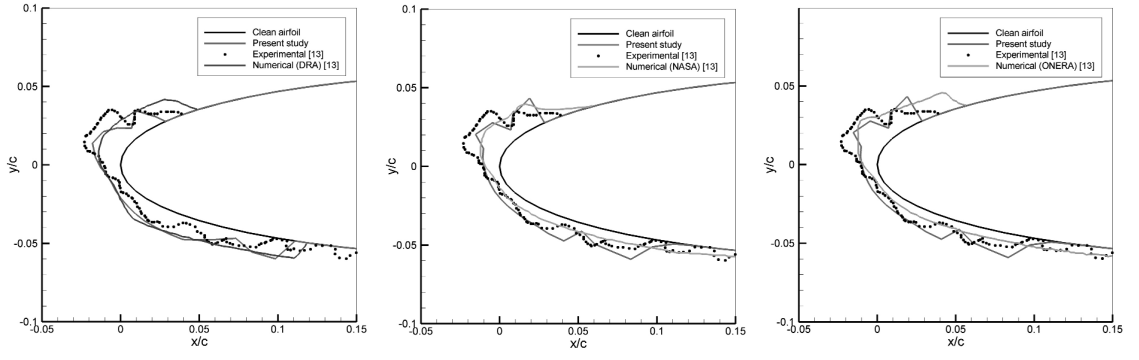

Figure 6. Comparison of experimental and numerical results with the present study (Case 31).

https://doi.org/10.1017/S000192400000525X Published online by Cambridge University Press

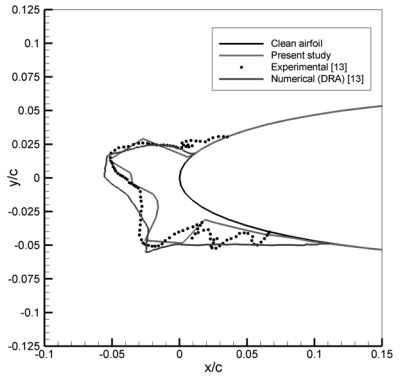

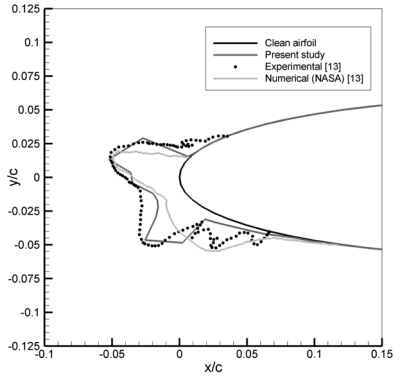

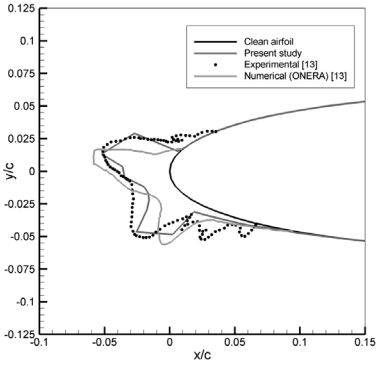

Figure 7. Comparison of experimental and numerical results with the present study (Case 34).

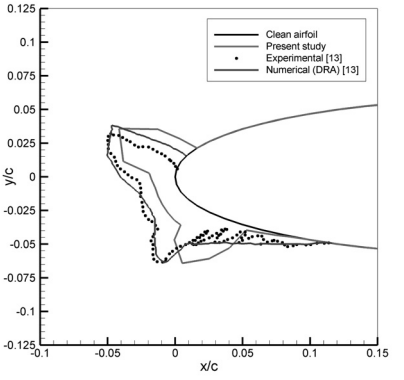

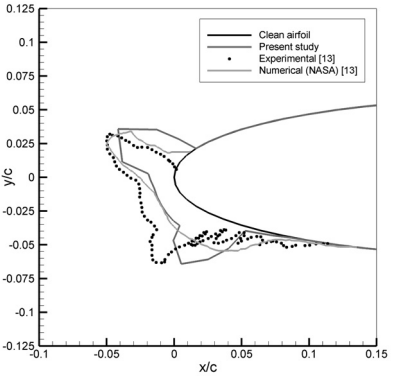

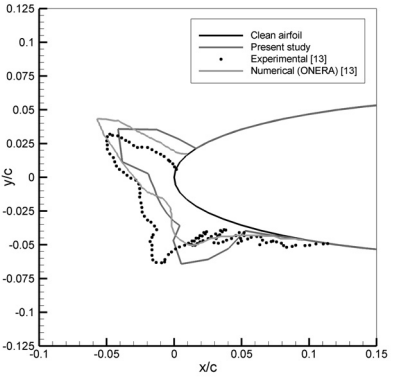

Figure 8. Comparison of experimental and numerical results with the present study (Case 35).

In Fig. 7, another glaze ice case is shown, this time with a lower temperature. The experimental ice shape displays two horns, with almost equal sizes. As can be seen, all the numerical computations including the current one slightly underestimate the iced region on the upper surface, while there is the current study provides a better agreement on the lower surface. The horns are predicted by the current study, also by the results of DRA and ONERA. Although the exact locations of the horns are almost perfectly predicted in the current study, their sizes are slightly overestimated. As a result, the total ice volume seems to be also slightly underestimated. For this case the maximum ice thickness is roughly 3cm occurring at the upper horn, corresponding to an intense icing condition.

https://doi.org/10.1017/S000192400000525X Published online by Cambridge University Press

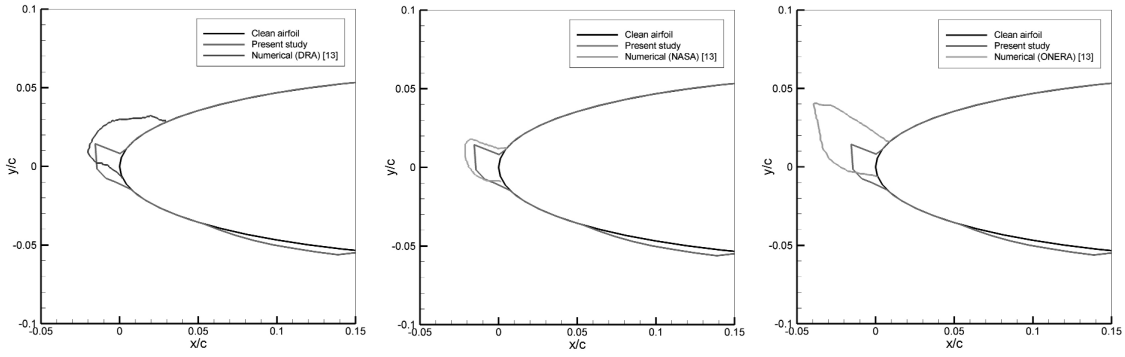

Figure 9. Comparison of experimental and numerical results with the present study (Case 39).

Figure 8 illustrates the results of another glaze ice case with a slightly higher temperature than the case in Fig. 7. Here, again two prominent horns are visible; however this time the horn on the upper surface is slightly longer in the experimental shape. All computational results including the current one slightly overestimate the iced region on the upper surface, while the match is also good on the lower surface. The big horn on the upper surface is well reproduced by the current study, with a slight mismatch in its exact location. The lower horn is also reproduced again with a small mismatch in its location. It can also be seen that the volume of ice is very well reproduced by the current study compared to the experimental shape. The thickness of ice remaining between the two horns is slightly underestimated by the current computations but the overall ice shape has been well captured. The maximum ice thickness is also about 3cm in this case, occurring at the upper horn again suggesting intense icing.

Figure 9 illustrates a case where the freestream velocity is high enough to render aerodynamic heating effects important. For this case, there are no experimental results available; however the agreement of the results of the current study with those of other computations, especially with those of NASA is good, shapewise in particular. For this case, although the extent of the aerofoil wetted by the incoming droplets is much larger than the region that is iced, aerodynamic heating raises the surface temperature of a large portion of the leading edge above the freezing temperature, preventing ice formation there. It is also noteworthy that the very thin layer of ice on the lower surface is not observed in any other computational result that is shown except the current study. The maximum ice thickness occurs at the bump at the leading edge and is about 1·1cm, which is in the border between moderate and intense icing when the exposure time is considered.

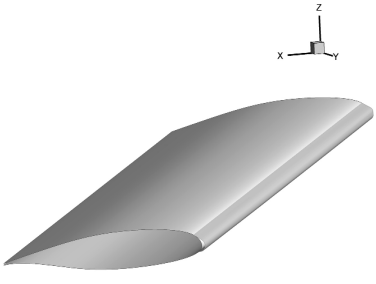

Figure 10. Ice formation at the leading edge of the NASA MS-317 30º swept wing, V_∞ = 74ms^{-1}, α = 4º, T_a = –18·1ºC.

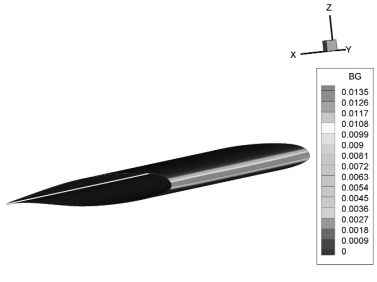

Figure 11. Ice thickness (in m) distribution over the NASA MS-317 30º swept wing, V_∞ = 74ms^{-1}, α = 4º, T_a = –18·1ºC.

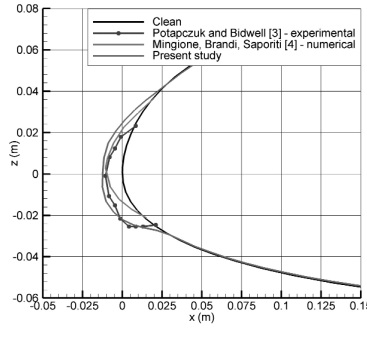

Figure 12. Comparison of ice shapes at the mid-semispan of the NASA MS-317 30º swept wing, V_∞ = 74ms^{-1}, α = 4º, T_a = –18·1ºC.

https://doi.org/10.1017/S000192400000525X Published online by Cambridge University Press

Table 3
Geometric characteristics and flow conditions for code validation (3D)

Variable	Value			
	Wing	Circular intake	Elliptical intake	Turboprop intake
α, angle-of-attack (º)	4	0	0	0
c, wing chord or duct length (m)	0·9	1·0	1·0	0·08m
b, wing span or duct diameter (m)	7·3	0·3	0·6	variable
V_∞, freestream velocity (ms^{-1})	74	75	75	75
p_∞, ambient pressure (Pa)	71,910	61,641	61,641	61,641
T_a, ambient temperature (ºC)	–18·1	–11·0	–11·0	–11·0
ρ_a, liquid water content (g/m^3)	1·0	2·58	2·58	1·0
t_{exp}, exposure time (s)	390	360	360	180
d_p, droplet diameter (μm)	20	15	15	15

Figure 10 shows the ice formation on the leading edge of the NASA MS-317 30° swept wing under the conditions given in the second column of Table 3. For these calculations 99 chordwise and ten spanwise panels are used. As can be seen, the ice shape is fairly uniform and has smooth contours, which is typical of rime ice. Figure 11 shows the ice thickness distribution. The maximum ice thickness is around 13·5mm (intense icing) and occurs near the leading edge. The ice thickness decreases smoothly in the streamwise direction.

Figure 12 shows the comparisons with numerical and experimental data for the same case, where ice shapes at mid-span are shown. As can be seen, although the present code estimates the overall ice shape fairly accurately, the ice thickness and the iced region are slightly overestimated, while the data of Mingione *et al*[4] shows a marked underestimation.

Judging from the results presented so far and their agreement with experimental results available in the literature, it can be said that the outlined method performs well but is not perfect in terms of accuracy from the ice shapes and iced regions point of view. In order to improve the performance of the developed tool, one of the most obvious improvements would be to replace the semi-empirical approach employed for the calculation of the convective heat transfer coefficients with a higher order method, like a Navier-Stokes solver. This would actually serve two purposes since the results of the flow solver are also employed by the droplet trajectory calculations, although one expects a minor improvement in the latter.

Another improvement would be to treat the water flow on the surface as an additional problem with a higher order approach like the one studied by Myers, *et al*[15]. This would allow runback water effects to be simulated more faithfully, which are important for glaze ice conditions yielding irregular ice shapes. Nevertheless, both this and the previously suggested improvements would increase the computational immensely, rendering the current approach a good compromise between accuracy and speed.

4.0 RESULTS FOR OTHER GEOMETRIES

4.1 Circular and elliptical air intakes

The developed computer program is also capable of handling geometries other than wings like intakes and ducts. In this section, a circular and an elliptical intake geometry is analysed. Both of these geometries are generated for illustration purposes only and do not correspond to a real

https://doi.org/10.1017/S000192400000525X Published online by Cambridge University Press

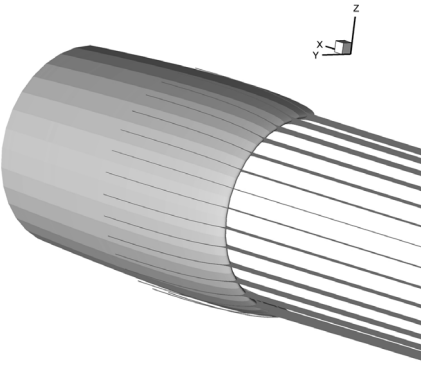

Figurex 13. Droplet trajectories around the circular intake, V_∞ = 75ms^{-1}, α = 0º, T_a = –11ºC.

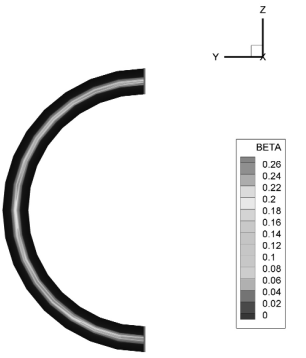

Figure 14. Droplet collection efficiency distribution on the circular intake, V_∞ = 75ms^{-1}, α = 0º, T_a = –11ºC.

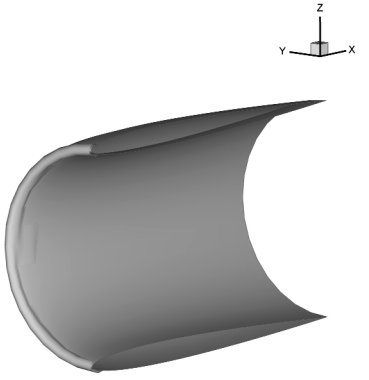

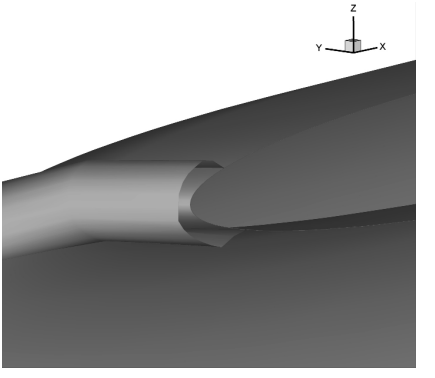

Figure 15. Ice formation at the leading edge of the circular intake, V_∞ = 75 ms^{-1}, α = 0º, T_a = –11ºC.

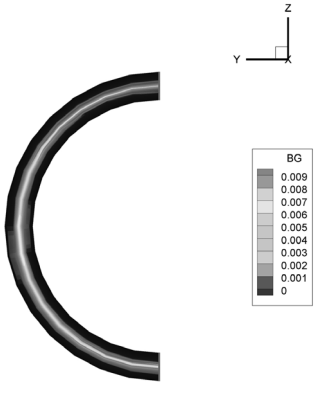

Figure 16. Ice thickness (in m) distribution over the circular intake, V_∞ = 75ms^{-1}, α = 0º, T_a = –11ºC.

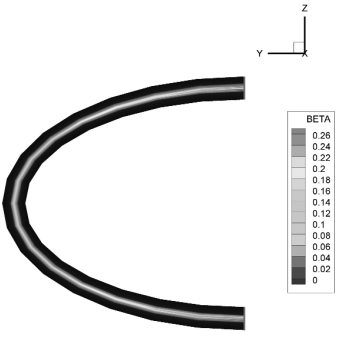

Figure 17. Droplet collection efficiency distribution on the elliptical intake, V_∞ = 75ms^{-1}, α = 0º, T_a = –11ºC.

configuration although they closely resemble typical commercial transport aircraft turbofan engine nacelles. Both geometries are created by wrapping a NACA 0006 aerofoil to form a closed geometry. The duct lengths are 1m for both geometries and the aspect ratio of the elliptical geometry is 2:1. In the computations, 149 chordwise and 16 circumferential panels are used both for the circular and elliptical intake geometries. 199 chordwise and 16 circumferential panels are also tested but no significant variation in the results are observed.

https://doi.org/10.1017/S000192400000525X Published online by Cambridge University Press

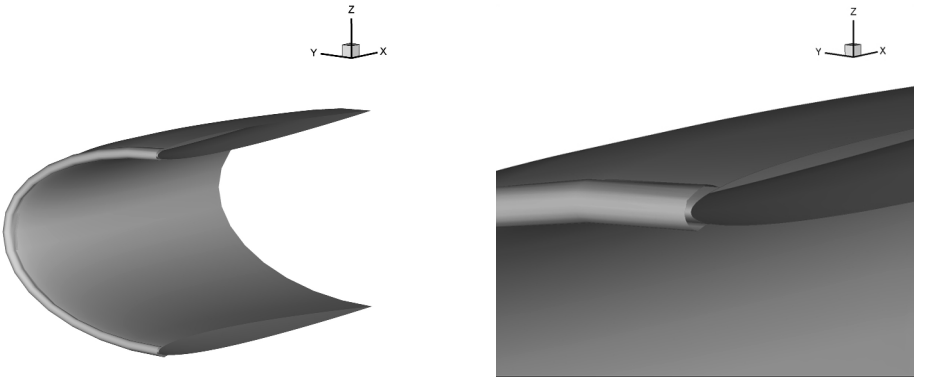

Figure 18. Ice formation at the leading edge of the elliptical intake, V_∞= 75ms^{-1}, α = 0º, T_a = –11ºC.

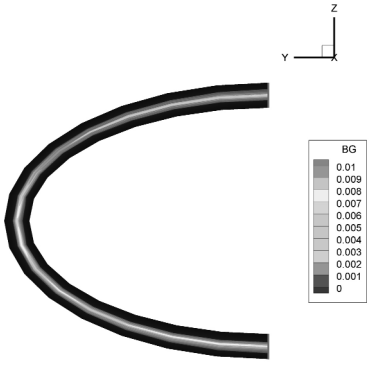

Figure 19. Ice thickness (in m) distribution over the elliptical intake, V_∞= 75ms^{-1}, α = 0º, T_a = –11ºC.

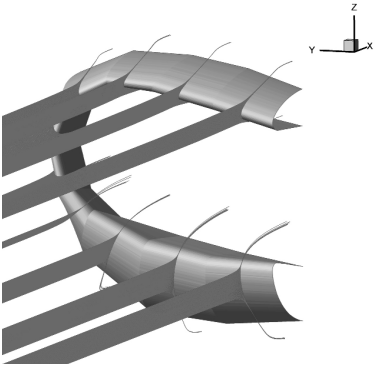

Figure 20. Droplet trajectories around a turboprop air intake, V_∞ = 75ms^{-1}, α = 0º, T_a = –11ºC.

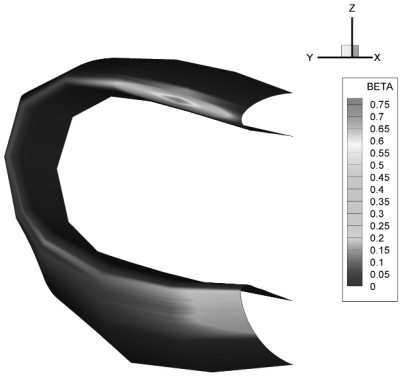

Figure 21. Droplet collection efficiency distribution on the turboprop air intake, V_∞ = 75ms^{-1}, α = 0º, T_a = –11ºC.

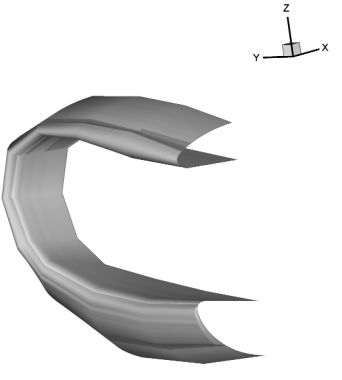

Figure 22. General view of the ice formation at the leading edge of the turboprop air intake, V_∞ = 75ms^{-1}, α = 0º, T_a = –11ºC.

Figure 13 shows the droplet trajectories around the circular geometry, while Fig. 14 illustrates the droplet collection efficiency distribution. As can be seen, the droplet collection efficiency distribution is fairly uniform and the highest droplet collection efficiency, which is around 0·26 occurs around the leading edge. This is smaller than the corresponding value for the wing geometry analysed previously. This implies that the circular intake constitutes a larger obstacle

https://doi.org/10.1017/S000192400000525X Published online by Cambridge University Press

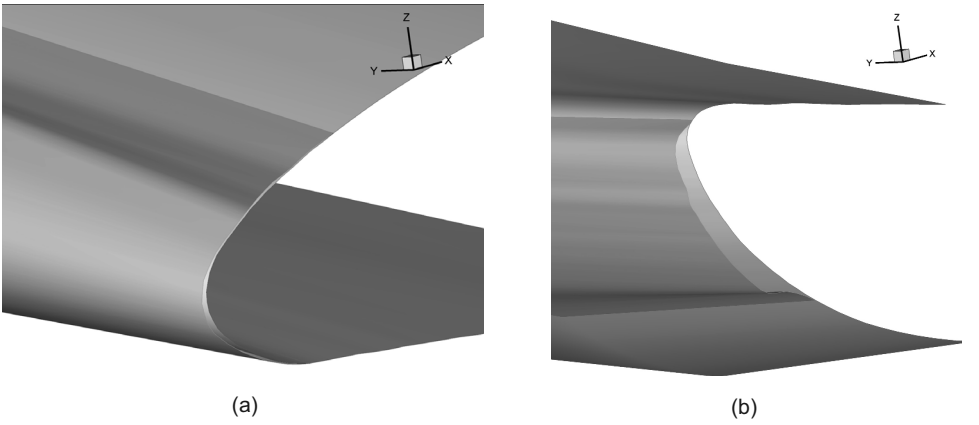

(a) (b)

Figure 23. Details of the ice formation at the (a) upper and (b) lower lips of the turboprop air intake, $V_\infty = 75ms^{-1}$, $\alpha = 0º$, $T_a = -11ºC$.

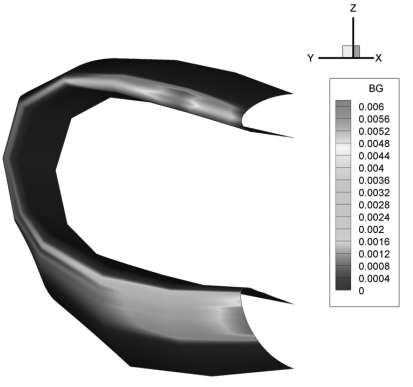

Figure 24. Ice thickness (in m) distribution over the turboprop air intake, $V_\infty = 75ms^{-1}$, $\alpha = 0º$, $T_a = -11ºC$.

compared to the wing, so that the droplets are diverted away from the body, although the cross-sectional properties of the two geometries are similar to each other.

Figures 15(a) and 15(b) show the general and detailed layout of the ice shape that forms around the leading edge. The uniformity of the ice shape is immediately noticeable. However, the ice thickness is not maximum at the leading edge, suggesting that there is runback water effect, implying glaze ice formation. Finally, Fig. 16 shows the ice thickness distribution, which strengthens the above inferences. The maximum ice thickness is below 10mm (moderate icing intensity), which is less than the value for the wing geometry analysed previously.

The collection efficiency distribution around the elliptical geometry is presented in Fig. 17. The distribution is not uniform, the highest values being attained towards the centreline of the intake. Compared to the circular intake, the collection efficiency values are comparable but they are still less than those for the wing geometry.

Figure 18 shows the ice shapes that form at the leading edge. The shapes suggest that there is some runback water effect, implying glaze ice formation. These shapes are almost identical to the ones obtained for the circular geometry, which is mostly due to identical flow and icing conditions. Ice thickness distribution is depicted in Fig. 19, where the highest values are obtained towards the centreline. The highest ice thickness is around 10mm, which is comparable to the value for the circular intake and again corresponding to moderate icing conditions when the exposure time is considered.

https://doi.org/10.1017/S000192400000525X Published online by Cambridge University Press

4.2 A turboprop trainer air intake

This section illustrates the capability of the developed computer program to analyse the ice formation around highly irregular and complex geometries. The geometry that is analysed is an air intake of a turboprop trainer aircraft.

Figure 20 shows the droplet trajectories obtained for this geometry, where the complexity of the geometry and the trajectory pattern are visible. Figure 21 shows the corresponding droplet collection efficiency distribution pattern, which is highly irregular. Away from the centreline, the efficiency values fall almost to zero, while they attain values around 0·8 at the upper lip of the intake slightly outboard of the centreline.

Figure 22 shows the general view of the ice formation around the leading edge of the intake, which is again highly irregular. Figures 23(a) and (b) illustrate the details of the ice shape at the upper and lower lips of the intake around the centreline. At the lower lip of the intake, the ice is considerably thick (around 5-6mm as can be seen from Fig. 24) and occupies a large part of the lower part of the intake, mainly due to runback water. At the upper lip, the ice thickness is again around 6mm close to the centreline but this reduces rapidly to almost zero exactly at the centreline. Ice occupies a much smaller area suggesting that runback water effect is less, meaning that the ice that forms is mainly rime ice. However, the exposure time and the thickness of ice that accumulates during exposure correspond to intense icing conditions.

5.0 CONCLUSIONS

Ice shape and ice mass predictions are performed over various aerofoil/wing and intake geometries using the Extended Messinger Model extended to three dimensions. The validation study indicates that the developed tool is capable of satisfactorily predicting ice shapes including glaze ice shapes with highly irregular contours with single or double horns. The iced regions and ice volumes are also fairly well predicted by the developed tool. Considering that most of the selected test cases correspond to intense icing conditions where the ice accumulation rate is extremely high, the success of the developed tool can be better appreciated.

An important inference of the study is that although the collection efficiency levels are less than those of wing geometries, intake or duct geometries experience important ice accumulation. When the sizes of these geometries are considered, it is obvious that intake geometries are as prone to icing as wing geometries. More severe icing conditions than the ones studied here could result in severe blockage of the intake, resulting in power fallbacks.

It is also shown that irregular geometries with largely varying thicknesses and contours are also within the capabilities of the developed tool. Irregular droplet impact patterns and resulting droplet collection efficiencies together with the ice shapes can be successfully computed.

The developed tools could be easily modified and used for determining the capacities of a heated anti/de-icing leading edge device, and also for certification and design purposes.

For further studies, the droplet trajectories could be calculated using a parallel computing approach, which would significantly reduce the run time since almost 99% of all computational time is spent for the droplet trajectories alone.

Also, the icing module of the code can be coupled with different flow solvers allowing the investigation of not only airframe components alone but the entire flying vehicle.

https://doi.org/10.1017/S000192400000525X Published online by Cambridge University Press

REFERENCES

1. ÖZGEN, S. and CANIBEK, M. Ice accretion simulation on multi-element aerofoils using extended Messinger model, *Heat and Mass Transfer*, 2009, **45**, (3), pp 305-322.
2. MYERS, T.G. Extension to the messinger model for aircraft icing, *AIAA J*, 2001, **39**, pp 211-218.
3. POTAPCZUK, M.G. and BIDWELL, C.S. Swept wing ice accretion modeling, NASA TM-103114, 1990.
4. MINGIONE, G., BRANDI, V. and SAPORITI, A. A 3D Ice accretion simulation code, AIAA Paper 99-0247, 1999.
5. CEBECI, T. and BESNARD, E. Prediction of the performance degradation of aircraft in natural icing conditions, AIAA Paper 94-0487, 1994.
6. PAPADAKIS, M., WONG, S.-C., RACHMAN, A., HUNG, K.E., VU, G.T. and BIDWELL, C.S. Large and small droplet impingement data on aerofoils and two simulated ice shapes, NASA TM-2007-213959, 2007.
7. KATZ, J. and PLOTKIN, A. *Low-Speed Aerodynamics*, 2nd ed, Cambridge University Press, Cambridge, UK, 2001.
8. PARASCHIVIOU, I. and SAEED, F. *Aircraft Icing*, 2007 (unpublished book draft).
9. CARUSO, S.C. NEARICE: An Unstructed-Mesh Navier-Stokes-Based Ice Accretion Prediction Method, AIAA Paper 94-0606, 1994.
10. JECK, R.K. Meteorological data for use in simulation icing conditions in Ice Accretion Simulation, AGARD-AR-344, 1997.
11. CLIFT, R., GRACE, J.R. and WEBER, M.E. *Bubbles, Drops and Particles*, Academic Press, New York, USA, 1978.
12. SCHLICHTING, H. *Boundary Layer Theory*, 7th ed, McGraw-Hill, New York, USA, 1979.
13. WRIGHT, W.B., GENT, R.W. and GUFFOND, D. DRA/NASA/ONERA collaboration on icing research, part II- prediction of aerofoil ice accretion, NASA CR-202349, 1997.
14. GENT, R.W., DART, N.P. and CANSDALE, J.T. Aircraft icing, Phil Trans R Soc Lond A, 2000, 358, pp 2873-2911.
15. MYERS, T.G., CHARPIN, J.P.F. and THOMPSON, C.P. Slowly accreting ice due to supercooled water impacting on a cold surface, *Phys Fluids*, 2002, **14**, (1), pp 240-256.
16. FORTIN, G., LAFORTE, J.-L. and ILINCA, A. Heat and mass transfer during ice accretion on aircraft wings with an improved roughness model, *Int J Thermal Sciences*, 2006, **45**, pp 595-606.